

## Heat and Freshwater Transport by Mesoscale Eddies in the Southern Subpolar North Atlantic

Vasco Müller<sup>1,2,3</sup> , Dagmar Kieke<sup>1,2</sup> , Paul G. Myers<sup>4</sup> , Clark Pennelly<sup>4</sup> ,  
 Reiner Steinfeldt<sup>1,2</sup> , and Ilaria Stendardo<sup>2</sup> 

<sup>1</sup>MARUM-Center for Marine Environmental Sciences, University of Bremen, Bremen, Germany, <sup>2</sup>Institute of Environmental Physics (IUP), University of Bremen, Bremen, Germany, <sup>3</sup>Now at International Pacific Research Center, University of Hawai'i, Honolulu, HI, USA, <sup>4</sup>Department of Earth and Atmospheric Sciences, University of Alberta, Edmonton, Alberta, Canada

### Key Points:

- The Gravest Empirical Mode technique allowed to reconstruct profiles of hydrographic properties for mesoscale eddies in the North Atlantic
- Hydrographic and altimeter-derived data and model output served to quantify heat and freshwater transports of eddies crossing 47°N
- Northward moving cold/fresh cyclones from the Western Boundary Current contribute considerably to the heat/freshwater transports by eddies

### Correspondence to:

V. Müller,  
 vmueller@hawaii.edu

### Citation:

Müller, V., Kieke, D., Myers, P. G., Pennelly, C., Steinfeldt, R., & Stendardo, I. (2019). Heat and freshwater transport by mesoscale eddies in the southern subpolar North Atlantic. *Journal of Geophysical Research: Oceans*, 124, 5565–5585. <https://doi.org/10.1029/2018JC014697>

Received 19 OCT 2018

Accepted 11 JUN 2019

Accepted article online 20 JUN 2019

Published online 7 AUG 2019

**Abstract** A new data set of temperature and salinity fields reconstructed from satellite altimetry data between January 1993 and April 2014 is combined with satellite observations of mesoscale eddies in the subpolar North Atlantic between 40°N–55°N and 43°W–20.5°W. The data set is used to calculate the meridional heat and freshwater transports related to the propagation of eddies crossing 47°N, a latitude close to the boundary between the subpolar and the subtropical gyres. The largest heat and freshwater transports by eddies are observed in the western part of the Newfoundland Basin. Around 35–45% of the heat and freshwater transports by eddies across 47°N stem from individual isolated eddies with large thermohaline signatures. Northward moving cold and fresh cyclonic eddies carrying subpolar water from the Western Boundary Current make a considerable contribution to the overall heat and freshwater transport by eddies crossing 47°N. While the transport by individual eddies is negligible compared to the transport by the mean flow in this region, it can have a notable influence on the temporal variability. The analysis is repeated for a model simulation with 1/12° horizontal resolution for the period 2002–2013. The observed results are well reproduced in the model simulation; in particular, the modeled number of eddies crossing 47°N, the spatial distribution, and the associated heat and freshwater transports across this latitude are consistent with the observations.

### 1. Introduction

Mesoscale eddies in the ocean, with a typical size of  $\mathcal{O}(100\text{ km})$  and a typical lifetime in the order of several days to several months, cover around 25–30% of the ocean surface at any given moment (Chaigneau et al., 2009). For most of the world's ocean, the kinetic energy of these mesoscale features is larger than the kinetic energy of the mean flow, inducing local exchange and horizontal mixing of water masses from different origin and of different properties. Individual eddies can also carry water trapped inside their cores and transport the properties of these waters (e.g., temperature, salinity, oxygen, or nutrients) over long distances (Robinson, 1983; Waugh & Abraham, 2008). Therefore, eddies are believed to play an important role for the horizontal transport of mass, heat, and salt throughout the ocean (e.g., Wunsch, 1999).

Sea level anomaly (SLA) observations obtained from satellite altimetry provide the means of identifying and tracking eddies using automated algorithms (e.g., Chaigneau et al., 2008; Chelton et al., 2011; Nencioli et al., 2010). Combining these with sea surface temperature and salinity observations from satellites allows to analyze their surface signatures (e.g., Melnichenko et al., 2017) and to quantify horizontal surface fluxes (Müller et al., 2017). However, investigating the vertical structure of eddies and quantifying the respective heat and freshwater transports associated with the eddies are more challenging due to the lack of adequate subsurface observations on mesoscale resolutions. A promising method in recent years has been using data from Argo floats, autonomous profiling floats that measure the temperature and salinity of the upper 2,000 m of the ocean (Argo, 2000). Combining remote sensing measurements with observations from Argo floats has allowed for studying the mean vertical structure of eddies (Chaigneau et al., 2011; Keppler et al., 2018; Pegliasco et al., 2015), as well as their average transports of mass, heat, and salt content on global (Dong et al., 2014; Zhang et al., 2014) and regional scales (Amores et al., 2017; Dong et al., 2017; He et al., 2018). While the number of Argo floats in the world ocean has already increased to almost 4,000, their coverage is still too scarce to provide observations of every eddy detected at the

surface. All these studies therefore average over a large number of eddies to analyze the average characteristics and transports.

In this study, we present a different approach, using a new 3-D data set of temperature and salinity derived from satellite altimetry data following methods outlined by Stendardo et al. (2016). The data set is inferred from applying the Gravest Empirical Mode (GEM) technique to Argo data and constructing a transfer function between temperature/salinity (T/S) profiles and dynamic height (Stendardo et al., 2016). The respective 3-D temperature and salinity fields are then parameterized as a function of the SLA obtained from satellite altimetry data. The GEM method has the advantage of covering the same period (1993–2014) with the same temporal (daily) and spatial ( $1/4^\circ \times 1/4^\circ$ ) resolution as the satellite altimetry data that have been used to detect the eddies. This allows for the calculation of the temperature and freshwater anomalies related to each observed eddy and the respective transports. In doing so, it is possible to address not only an estimate for an average transport by eddies but also the differences between individual eddies and the variability in the transports by eddies. However, the trade-off for using the new approach is that the T/S data are no longer true observed profiles but rather reconstructions based on the respective observed SLA.

Here, we focus on the western subpolar North Atlantic between  $40^\circ\text{N}$ – $55^\circ\text{N}$  and  $43^\circ\text{W}$ – $20.5^\circ\text{W}$ . In this region, cold and rather fresh water detaches from the Western Boundary Current (WBC), partially recirculating northward into the warm and salty North Atlantic Current (NAC) and interacting with the interior of the North Atlantic (Bower et al., 2009; Dutkiewicz et al., 2001; Kieke et al., 2009). Mesoscale eddies forming between the two current systems provide a mechanism for the local exchange of temperature in this region (Bower et al., 2013; Dutkiewicz et al., 2001; Müller et al., 2017). We detect individual cyclonic eddies (CEs) and anticyclonic eddies (AEs) crossing the latitude of  $47^\circ\text{N}$ , reconstruct the 3-D structure for these eddies, and determine and investigate the meridional heat and freshwater transports carried by these eddies across  $47^\circ\text{N}$ .

Complementary to the observations, we include model results from an ocean model simulation that is based on the Nucleus for European Modeling of the Ocean (NEMO) modeling framework. For this purpose we use the *Arctic Northern Hemisphere Atlantic* configuration ( $1/4^\circ$ ) with a nested  $1/12^\circ$  horizontal resolution encompassing the subpolar North Atlantic termed ANHA4-SPG12. Müller et al. (2017) have shown that the observed surface characteristics of eddies and their surface temperature fluxes are well reproduced in this configuration. The model simulation allows to analyze data that are completely independent from the GEM method and can therefore provide independent support showing that the results derived from the GEM method are robust. Furthermore, this is the first study focusing on the vertical structure of eddies in the ANHA4-SPG12 configuration and the respective heat and freshwater transports of these eddies. If the model proves to be a reliable tool to analyze eddy dynamics, it can be used in the future for studying regions that are not well suited for the construction of T/S profiles with the GEM method.

The following questions will be investigated:

1. Is the temperature and salinity data set derived from the GEM method suited for the analysis of mesoscale eddies?
2. What is the vertical thermohaline structure of mesoscale eddies in the subpolar North Atlantic covered by the data?
3. How large are the meridional heat and freshwater transports by individual eddies crossing  $47^\circ\text{N}$ ? How does this compare to the mean and turbulent components of the total transport across  $47^\circ\text{N}$ ?
4. How well are the eddy vertical structure and transports simulated in the NEMO model?

## 2. Data

We identified surface signatures of individual eddies from geostrophic velocity fields derived from the mapped *all-sat-merged* delayed time mapped SLA data set (DT-MSLA), version 15.0, provided by Archiving, Validation and Interpretation of Satellite Oceanographic data (AVISO) (<http://www.aviso.altimetry.fr/duacs/>). The SLA observations stem from the SSALTO/Duacs multimission altimeter product (Ducet et al., 2000; Le Traon et al., 1998). The considered SLA fields were mapped on a  $1/4^\circ \times 1/4^\circ$

Mercator grid with a daily resolution for the considered period January 1993 to April 2014. The anomalies in the data set were calculated with respect to the 20-year mean for the years 1993 to 2012 (SSALTO/Duacs, 2014). The SLA is also used to reconstruct the 3-D salinity and temperature fields using the GEM method described in the section below. Geostrophic velocity anomalies ( $u$ ,  $v$ ) derived from each SLA map are also provided by AVISO. For the eddy detection, we are interested in intraseasonal changes of the velocity field. Hence, the mean annual cycle for each velocity component was calculated at every grid point and subtracted from the original velocity field.

The required Argo data for the North Atlantic used to construct the GEM and for the evaluation of the method were downloaded from the Coriolis data center and provided in a quality-controlled form by B. Klein (personal communication, Federal Maritime and Hydrographic Agency, Hamburg, Germany). This particular data set covers the period 2003–2011.

In this study, we use an updated version of the 3-D data set created by Stendardo et al. (2016) with the GEM technique to provide daily data for temperature and salinity ranging from 1993 to 2014 with a spatial resolution of  $1/4^\circ \times 1/4^\circ$  and 10-dbar vertical resolution. Even though temperature and salinity data are not measured directly, we will use the term observations (in contrast to model results) in the following to describe the results derived from the GEM data. A detailed description of the method and its evaluation has been provided by Stendardo et al. (2016); here we will only summarize briefly the method and describe the differences from the previous version in section 4.2.

### 3. Model Configuration

The model simulation analyzed in this study is carried out with a nested  $1/12^\circ$  Arctic Northern Hemisphere Atlantic Subpolar Gyre (ANHA4-SPG12) configuration of the NEMO model numerical framework version 3.4 (Madec, 2008). The model setup is the same as in Müller et al. (2017), so we will only briefly describe the configuration here.

The  $1/12^\circ$  horizontal resolution configuration is two-way nested into the  $1/4^\circ$  ANHA4 configuration using the Adaptive Grid Refinement In Fortran tool (Debreu et al., 2008). The high-resolution nest covers the subpolar gyre region between  $36^\circ\text{N}$  and  $70^\circ\text{N}$ , with a zonal extent from  $0^\circ\text{W}$  to  $60^\circ\text{W}$  south of Newfoundland and around  $70^\circ\text{W}$  in the northern Labrador Sea (Figure 1). The ANHA4 configuration covers the whole North Atlantic and the Nordic Sea (including the Gulf of Mexico in the west and the Mediterranean Sea in the east) with open boundaries at  $20^\circ\text{S}$  and in the Bering Strait.

The ocean model includes the 3-D, linear free surface, hydrostatic, primitive equations coupled to the *Louvain-la-Neuve sea-ice model* (LIM2; Fichefet & Maqueda, 1997). The model consists of 50 vertical levels with 1-m thickness for the top layer and decreasing vertical resolution with depth. The sea ice module has an elastic-viscous-plastic ice rheology (Hunke & Dukowicz, 1997) with no-slip lateral boundary conditions for the sea ice and free-slip lateral boundary conditions for the ocean.

The open boundary conditions are provided from the Global Ocean Reanalyses and Simulations (GLORYS2v3) reanalysis obtained from MERCATOR (Ferry et al., 2010). The initial conditions for the model simulation stem from the same reanalysis product.

Vertical mixing at subgrid scales is parameterized using a turbulent kinetic energy closure model (Madec, 2008). For lateral mixing the model uses a bi-Laplacian operator with an eddy viscosity of  $1.0 \times 10^{10} \text{ m}^4/\text{s}^2$ . Subgrid-scale tracer lateral diffusion is parameterized with an isopycnal Laplacian operator with a horizontal eddy diffusivity of  $50 \text{ m}^2/\text{s}$ .

The model is forced with atmospheric data from the Canadian Meteorological Centre's Global Deterministic Prediction System Reforecasts (Smith et al., 2014), with 1-hr temporal resolution and a horizontal resolution of  $0.45^\circ$  longitude and  $0.3^\circ$  latitude. Runoff forcing is obtained from a monthly runoff climatology by Dai et al. (2009), manually remapped to the model grid to preserve runoff and watershed volumes (personal communication, X. Hu, University of Alberta, 2015). No relaxation is applied to the model salinity during the simulation. The model time step is 180 s, and the output is saved as 5-day averages for the period January 2002 to December 2013.

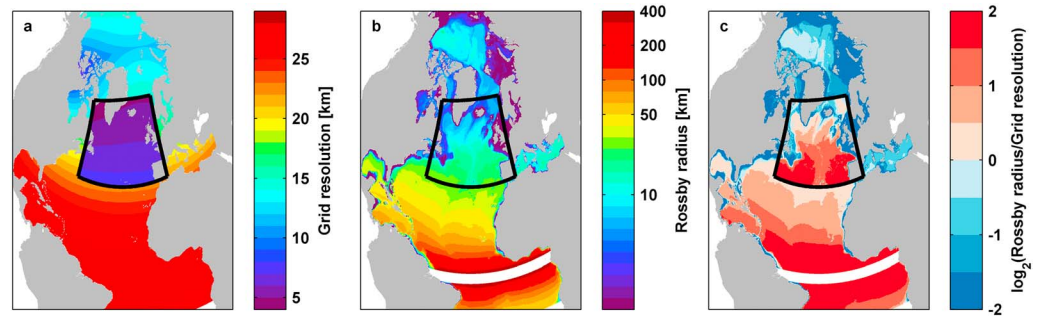


**Figure 1.** Horizontal grid resolution (average of  $X$  and  $Y$  directions) of the ANHA4-SPG12 subdomain in the subpolar gyre region (a), the respective Rossby radius (b), and the Rossby radius relative to the mesh resolution in  $\log_2$  (c). The model is eddy resolving for values above 1 (i.e., at least two grid points per Rossby radius, dark red) and eddy permitting for values between 0 and 1 (i.e., at least one to two grid points per Rossby radius, light red); eddies are not explicitly resolved for values below 0 (i.e., less than 1 grid point per Rossby radius, blue).

## 4. Methods

### 4.1. Automatic Detection of Individual Eddies

We use the vector-geometry-based algorithm by Nencioli et al. (2010) to detect and track eddies in the observations and the model simulations. The algorithm finds eddy centers by directly analyzing the velocity field and checking for rotating features. Before applying the algorithm, the velocity fields from the observations were linearly interpolated from  $1/4^\circ \times 1/4^\circ$  to  $1/6^\circ \times 1/6^\circ$  resolution. This did not change any features in the velocity field while improving the algorithm's performance (Liu et al., 2012; Müller et al., 2017). In the model simulation no further refinement was necessary since the grid had already a resolution of  $1/12^\circ \times 1/12^\circ$ . The outer boundary of each eddy was defined as the largest closed contour of the local stream function around the eddy center. The detected eddies were then tracked through time to determine the eddies' trajectories. Eddies with a radius smaller than  $R_{E_{\min}} = 20 \text{ km} \times \cos(\Phi)$ , where  $\Phi$  is the latitude of the eddies' center, or eddies with a lifetime of less than 1 week are not considered for further analysis.

A full description of the algorithm as used here is given by Nencioli et al. (2010), and the main steps are summarized by Liu et al. (2012) and Müller et al. (2017).

### 4.2. Reconstruction of 3-D Fields of Temperature and Salinity From the GEM Method

The GEM technique has its origin in constructing density profiles from acoustic traveltimes retrieved from bottom-mounted inverted echo sounders. The technique works particularly well in regions of strong horizontal density gradients such as the NAC, where it has been applied to calculate mean transports of the NAC (e.g., Meinen & Watts, 2000; Pérez-Brunius et al., 2004; Roessler et al., 2015). It has also been used to study the subsurface structure of the temperature and salinity fields in the Southern Ocean (Meijers et al., 2011; Swart et al., 2010) and in the subpolar North Atlantic (Stendardo et al., 2016). The method exploits the relationship between T/S profiles from, for example, quality-controlled Argo observations and dynamic height in order to parameterize the hydrographic structure as a function of the dynamic height from satellite altimetry (e.g., Meijers et al., 2011; Meinen & Watts, 2000; Stendardo et al., 2016). This means that the GEM is the first empirical mode of a hydrographic parameter in relation to the dynamic height.

For the analysis here, three regional boxes defined and separately studied by Stendardo et al. (2016); see their Figure 1) were merged into one single box: (1) the western Newfoundland Basin (extended slightly to the west in order to better capture the WBC), (2) the eastern Newfoundland Basin, and (3) the Rockall Trough region. In the overlapping areas between the regions, the values from both fields are linearly interpolated. The interpolation weight from the western region decreases linearly eastward from 1 to 0, and the weight from the eastern region increases accordingly.

The merged temperature and salinity fields are defined in a box ranging from  $44.625^\circ\text{W}$ – $17.625^\circ\text{W}$  and from  $45.125^\circ\text{N}$ – $49.875^\circ\text{N}$ , reaching down to 1,900 dbar, which is the reference pressure for the calculation of dynamic height from Argo data. Therefore, GEM data cannot be obtained in regions shallower than

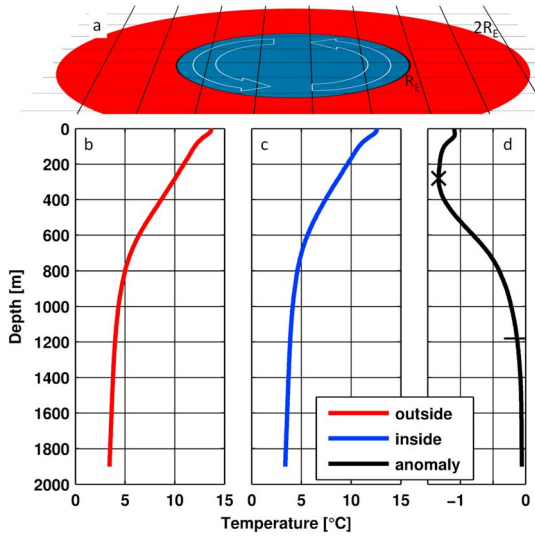


**Figure 2.** (a) Area outside (red) and inside (blue) of a CE with the corresponding averaged potential temperature profiles (b) outside and (c) inside of the eddy and (d) the respective temperature anomaly profile (inside-outside). The maximum temperature anomaly (mark at 280 m) is used to calculate the vertical extent of the eddy (horizontal line at 1,180 m).

~2,000 m. The section at 47°N is therefore not fully covered by the reconstructed temperature and salinity fields. The western part of the transect including the shelf is too shallow. The eastern part is also not suited due to water masses intruding from the Mediterranean Sea that weaken the informational value inferred from the GEM data, as explained by Stendardo et al. (2016).

### 4.3. Calculation of Heat and Freshwater Transports Related to Individual Eddies

The 3-D temperature and salinity fields reconstructed from the GEM method are used to calculate heat and freshwater transports associated with individual eddies identified from satellite altimetry. For the model simulation, the model fields are used for the calculation. Freshwater is defined with respect to a reference salinity:  $FW = \frac{S_{ref} - S}{S_{ref}}$ , where  $S_{ref} = 34.8$ , a typical reference value for the North Atlantic and Arctic Ocean (e.g., Dickson et al., 2007; Mertz et al., 1993).

The meridional heat transport  $F_H$  for each 3-D eddy is calculated as

$$F_H = v_E 2R_E c_{p0} \int_{H_E}^0 [\bar{\rho}(z) \overline{T'}(z)] dz, \quad [W] \quad (1)$$

where  $v_E$  is the eddy's average meridional translation velocity derived from the meridional displacement of the eddy over its lifespan,  $R_E$  is the radius of the individual eddy,  $c_{p0} = 4,200 \text{ J kg}^{-1} \text{ K}^{-1}$  is the average specific heat capacity,  $\bar{\rho}(z)$  is the average density profile calculated from the respective temperature and salinity profiles inside the eddy, and  $\overline{T'}(z)$  is the average temperature anomaly profile of the eddy.

The meridional freshwater transport  $F_{FW}$  for each 3-D eddy is calculated as

$$F_{FW} = v_E 2R_E \int_{H_E}^0 \overline{FW'}(z) dz, \quad \left[ \frac{m^3}{s} \right] \quad (2)$$

where  $\overline{FW'}(z)$  is the average freshwater anomaly profile of the eddy.

The average temperature/freshwater anomaly profiles are calculated as the difference between the average temperature/freshwater profile inside the eddy (Figure 2a, blue area and profile in Figure 2c) and outside the eddy (Figure 2a, red area and profile in Figure 2b). The outside area is defined as a ring around the eddy with a radius of twice the eddy's radius ( $R_E$ ).

The temperature anomaly profile (Figure 2d) is also used to determine the vertical extent of the respective eddy ( $H_E$ ).  $H_E$  is defined as the depth where the maximum temperature anomaly associated with the eddy has dropped by a factor of 10, that is,  $H_E = h \left( \frac{1}{10} |\overline{T'_{max}}| \right)$ , where  $|\overline{T'_{max}}|$  is the maximum anomaly of the temperature profile. If no vertical extent can be defined by this criterion (because the critical value is not reached),  $\frac{1}{n} |\overline{T'_{max}}|$ , with  $n = 9, 8, 7$ , etc. is used as critical values instead. If the critical value gets larger than  $\frac{1}{5} |\overline{T'_{max}}|$ , the vertical extent calculation is considered as failed, and the eddy is discarded from further analysis. Since the vertical grid of the data sets is in pressure coordinates, all fields first must be interpolated to a depth grid in the vertical direction in order to determine the transports by eddies.

Analyzing the vertical shape of the detected eddies with regard to lens, bowl, or cylinder shapes did not suggest to consider an additional coming scaling factors as was introduced by Dong et al. (2014). Using such a factor would only result in changing the respective transports by a constant factor but would not change the variability. We thus consider the vertical shape of the eddies to be cylindrical.

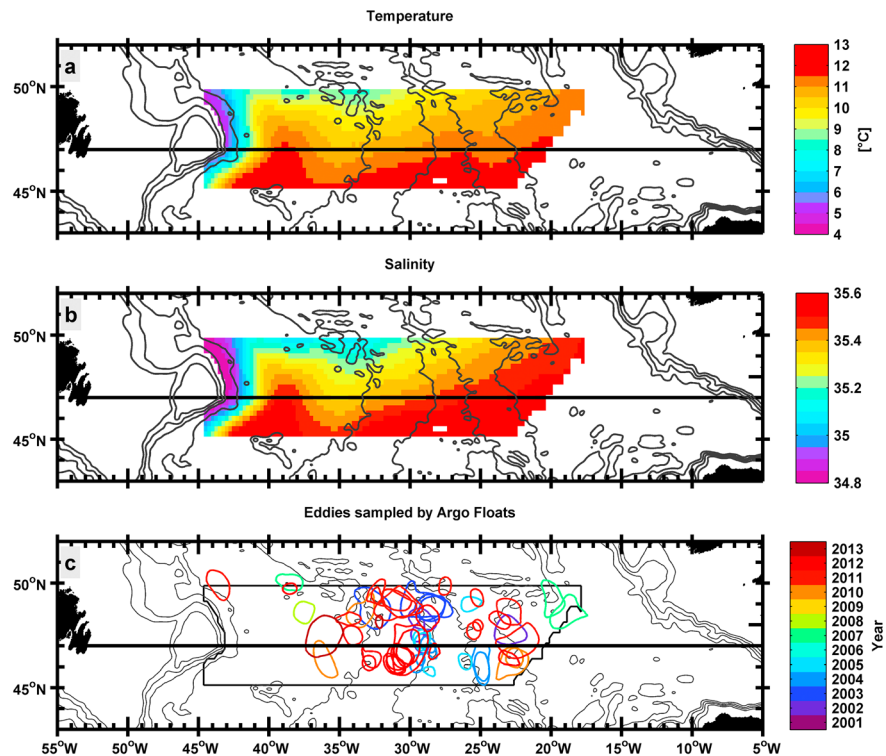


**Figure 3.** Average upper ocean (surface to 700 m) temperature (a) and salinity (b) of the GEM region for the period January 1993 to April 2014. The black line indicates the section at 47°N. Panel (c) shows all eddies that were sampled by Argo floats both inside the eddy boundaries and outside (compare Figure 1) within the GEM region (black box) between 2001 and 2013. Isobaths are given every 1,000 m using bathymetry derived from the ETOPO1 data set (Amante & Eakins, 2009). The bathymetry is low pass filtered to highlight general features.

The passing of an eddy over the 47°N line is related with a meridional volume transport. We thus are not able to calculate a total heat/freshwater transport for the eddies, but only the meridional transports of heat and freshwater anomalies trapped by eddies. In this interpretation, the eddy is only changing the temperature/salinity field, but not the transport. We will still use the terms heat/freshwater transport, since the analysis focuses on the amount of heat/freshwater transported by the propagation of individual eddies. The turbulent transports of heat and freshwater used later in section 5.5 (equations (3)–(4)) are physically different and represent transports of heat and freshwater for zero volume transport.

## 5. Results

### 5.1. Evaluation of the GEM Method With Application to Eddies

Stendardo et al. (2016) have provided an evaluation of the GEM method for seven different regions of the North Atlantic introduced in their paper. Figures 3a and 3b show the reconstructed temperature and salinity for the upper ocean in the merged GEM region used in the present study, averaged over the period January 1993 to April 2014. The meandering of the pathway of the NAC inferred from the spatial gradients of both fields can be clearly seen. In the following we will show that the GEM method is also useful for assigning temperature and salinity anomalies to individual eddies and thus infer respective heat and freshwater transports for 3-D eddies.

For the evaluation of the GEM method when applied to eddies, only those eddies with at least one Argo profile inside and outside of the eddy were considered. For this, every detected eddy was considered (and not just the ones tracked for at least 1 week). In the period covered by the considered Argo data, there were 16 CEs and 49 AEs in the GEM region that met the aforementioned conditions (Figure 3). Almost no eddies in the western Newfoundland Basin, where most eddies cross 47°N (Müller et al., 2017), were sampled by the required two Argo profiles in this period. The best coverage of eddies sampled with Argo profiles is after the

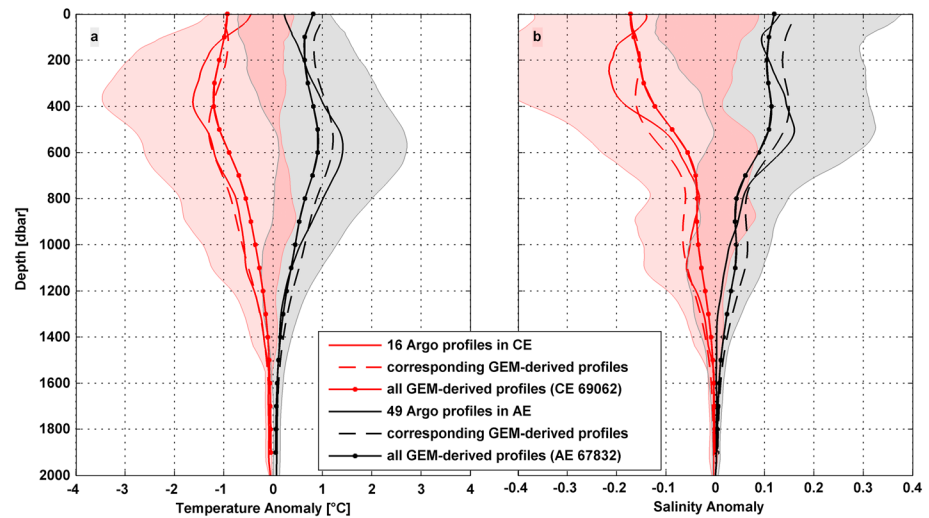


**Figure 4.** Mean temperature (a) and salinity (b) anomaly profiles (inside-outside eddy) for CE (red) and AE (black) sampled by Argo floats (solid lines), derived from the GEM corresponding with these particular Argo profiles (dashed lines) and from all GEM-derived profiles (line with markers, 69,062 profiles within CE and 67,832 profiles within AE) in the GEM region (see Figure 3). Note that typically, more than one GEM-derived profile is associated with CE/AE due to the horizontal dimension of the eddies. The shaded area represents one standard deviation of the Argo profiles. The profiles are smoothed with a 100-dbar running mean ( $\pm 50$  dbar).

year 2010. This is mainly because there are simply less Argo floats in the region before that time. The mean profiles of temperature and salinity anomalies (inside eddy-outside eddy) from Argo floats are reproduced reasonably by the GEM-derived hydrographic profiles (Figure 4).

For eddies sampled by Argo floats, there is an asymmetry between CE and AE when regarding the depth of the maximum of the average temperature and salinity anomaly profiles. The maximum temperature anomaly for the averaged Argo profiles is located at 380 m for CE and at 600 m for AE (Figure 4a). This

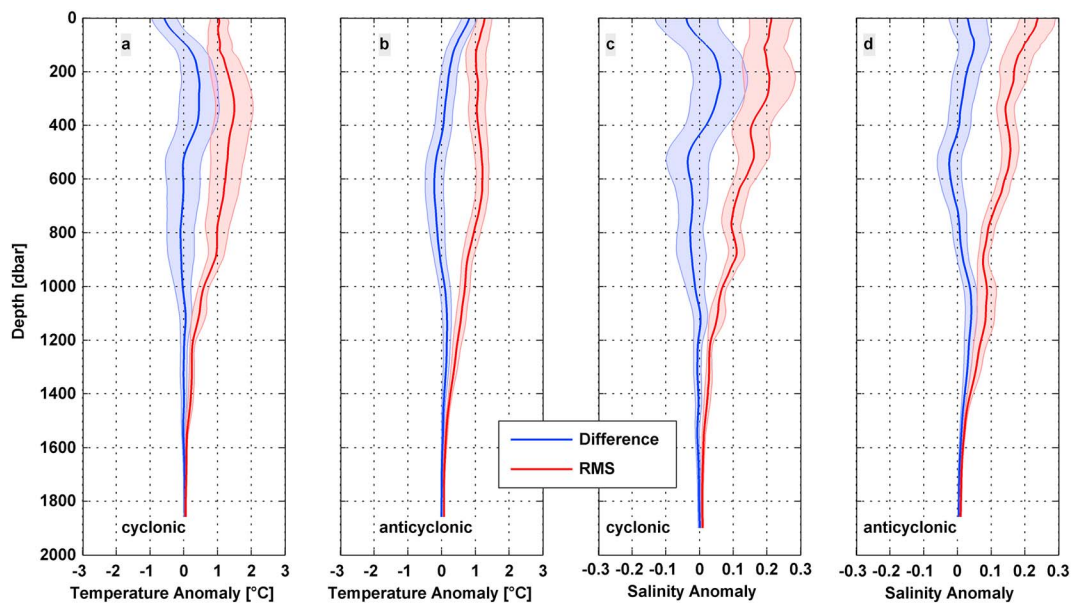


**Figure 5.** Mean temperature (a, b) and salinity (c, d) differences (red) and root-mean-square (RMS, blue) between the GEM-derived profiles and the corresponding profiles from Argo floats. CE (a, c) and AE (b, d) are regarded separately. The profiles are smoothed with a 100-dbar running mean  $\pm 50$  dbar. The shaded areas represent the 90% confidence intervals of the mean differences and RMS, respectively. They were computed by bootstrapping the mean difference and the RMS at each depth level with 1,000 iterations.

asymmetry is not well reproduced when looking at the average of the corresponding GEM-derived temperature anomaly profiles associated with these Argo profiles (500 m for CE and 540 m for AE). The same holds for the salinity profiles. For AE, the maximum salinity anomaly of the averaged Argo profile is more than twice as deep (500 m) than for CE (210 m). The asymmetry is not reproduced by the corresponding GEM-derived salinity anomaly profiles, where the maximum anomaly is located at the surface (Figure 4b).

Using all GEM-derived profiles associated with eddies (69,062 profiles in CE and 67,832 profiles in AE) instead of only the ones corresponding to individual Argo profiles leads to results closer to the Argo data. Again, every detected eddy (and not just the ones tracked for at least 1 week) was considered. The maximum temperature anomaly for the average of all CE is located at 360-m depth and the one for AE at 550-m depth. The pattern for salinity is not as clear with the salinity anomaly maximum of the averaged GEM-derived profiles located at the surface for both CE and AE (Figure 4b). However, the GEM-derived profile for AE shows a local salinity maximum at 420-m depth (black solid line in Figure 4b) and a saddle point at 210 m for CE. This behavior fits well to the observed Argo profiles (maxima at 500 and 210 m, respectively) and to the asymmetric behavior of CE and AE found in earlier studies (e.g., Dong et al., 2014, their Figure 2).

The different depths of the maximum anomaly for CE and AE can be explained by the eddies' effect on the underlying isopycnals. CEs lift the isopycnals, while AEs depress them. The CEs observed during a hydrographic cruise in the year 2015 described by Müller et al. (2017) lifted the isopycnals by roughly 500 m.

The temperature and salinity differences between GEM-derived profiles and the corresponding Argo profiles are largest between the surface and around 500-m depth, but all differences are lower than 1 °C and below 0.1 for salinity (Figure 5). The maximum root-mean-square residual (RMS) is between 1.3 and 1.5 °C for the temperature profiles and around 0.25 for salinity (Figure 5). Overall, the results for both the differences and RMS between GEM-derived profiles and corresponding Argo profiles are similar to the ones found by Stendardo et al. (2016) and show that the GEM method also works in the presence of eddies.

## 5.2. Heat and Freshwater Transports Carried by Eddies Across 47°N

Using 3-D temperature and freshwater data constructed with the GEM method allows for the first time to assign temperature and freshwater profiles to each individual 3-D eddy and to analyze the respective heat and freshwater transports across 47°N.

As introduced by Müller et al. (2017), eddies crossing 47°N are separated into *regular* and *strong eddies*, depending on the associated heat transport. The latter are defined as all those eddies with a heat transport that exceeds the mean transport plus twice the standard deviation in either direction ( $\overline{F_H} \pm 2\sigma(F_H)$ , where the overbar denotes the mean and  $\sigma$  is the standard deviation, Figure 6), all other eddies are defined as regular eddies. To account for the extreme values while calculating the standard deviations, the calculation is repeated 1,000 times with random subsamples of the time series, each with 1/3 of the length of the original time series, and then averaged. We use the heat transport to separate between strong and regular eddies, but using the freshwater transport instead would not make a difference (Figure 6). On average, a strong eddy ( $\overline{|F_{\text{strong}}|}$ ) accounts for more than 7 times of the heat and freshwater transport of regular eddies ( $\overline{|F_{\text{regular}}|}$ ).

All numbers displayed in the following paragraphs are given as a mean value, and the variability is represented by the inner quartile range (i.e., 50% of the values). The numbers and characteristics for the direct comparison (same zonal extent for observations and model and same time period) and full extent and full time period are all listed in Table 1.

In the observations between January 1993 and April 2014, a total of 415 eddies with a lifetime of more than 7 days and radius larger than  $R_{E_{\text{min}}} = 20 \text{ km} \times \cos\Phi$  were detected crossing 47°N in the region covered by the GEM field (Figures 6a and 6c). The mean net heat transport by eddies across 47°N ( $\overline{F_H}$ ) is significantly different from zero and directed southward (−2.1 TW). Freshwater transports are directed opposite of the heat transports (1.4 mSv). Twenty-six (i.e., 6.5%) of the 415 eddies crossing 47°N are strong eddies, making up for one third of the absolute heat and freshwater transports by eddies (i.e.,  $\sum |F_{H_{\text{strong}}}| / \sum |F_{H_{\text{all}}}|$ ).

The eddies detected in the ANHA4-SPG12 model simulation show similar characteristics as the observed eddies (Figures 6b and 6d). There are total of 357 eddies crossing 47°N from January 2002 to December 2013. The mean net heat transport across the full 47°N section in the model is southward (−1.9 TW), and

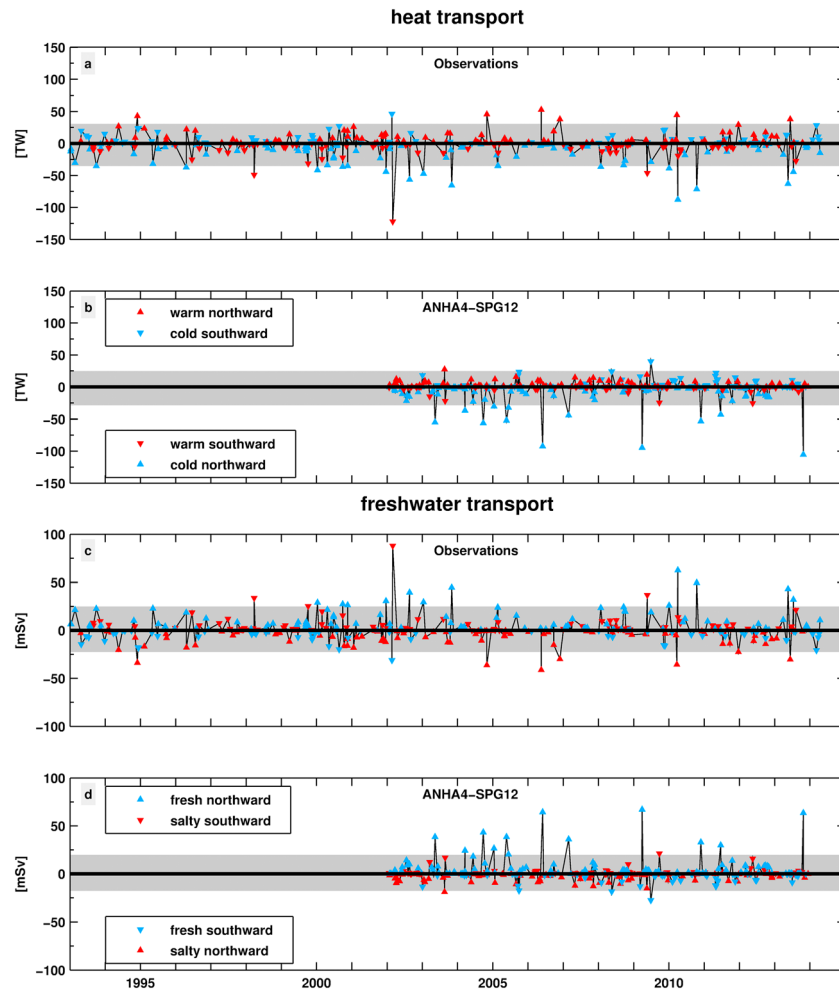


**Figure 6.** Time series of the meridional heat transport (a/b) and freshwater transport (c/d) by eddies across the zonal section at 47°N in the observations (a/c, only parts of the section are covered) and in the 1/12° ANHA4-SPG12 simulation (b/d, full section included),  $1 \text{ TW} = 10^{12} \text{ W}$ ,  $1 \text{ mSv} = 10^3 \text{ m}^3/\text{s}$ . Red (blue) triangles indicate eddies with a warm/salty (cold/fresh) anomaly. The direction of the triangle indicates the direction of meridional eddy movement across 47°N (northward/southward). The black line indicates the zero line, and the gray areas indicate 2 times the standard deviation of each time series around the mean. Note that the panels have different scales.

the mean net freshwater transport is northward (1.1 mSv). Out of the 357 eddies that cross 47°N in the model, only 14 (i.e., 3.9%) are strong eddies, accounting for 35% of the absolute heat and freshwater transports by eddies.

For the direct comparison of model and observations we focus on the zonal extent and the time period that are covered by both GEM field and ANHA4-SPG12 simulation (43°W–20.5°W, limited by the GEM region, and January 2002 to December 2013, limited by the model run). In this case there are actually more eddies in the 1/12° simulation (283) than in the observations (237) in that part of the 47°N section. Both heat and freshwater transports have the same directions as the observed transports and are significantly different from zero. The effect of strong eddies on the total heat and freshwater transport by eddies is lower in the model (35%) than in the observations (44%). Overall, an average strong eddy in the model accounts for more than 10 times of the thermohaline transport of an average regular eddy.

### 5.3. Vertical Structure of Eddies Crossing 47°N

Composites of the temperature and freshwater anomalies related to strong and regular eddies crossing 47°N are shown in Figures 7 and 8. The composites are constructed as follows: for every eddy, the

**Table 1**  
Number of Eddies Crossing 47°N and Their Respective Average Heat and Freshwater Transports

Period	Observations		Model (ANHA4-SPG12)	
	Jan 1993 to Apr 2014 (full period)	Jan 2002 to Dec 2013 (period as in the model)	Jan 2002 to Dec 2013 (model period)	Jan 2002 to Dec 2013 (model period)
Zonal extent of the 47°N section	43°W–20.5°W (western and central section)	43°W–20.5°W (western and central section)	43°W–20.5°W (section as in the observations)	53°W–10°W (full section)
Total number of eddies crossing 47°N	415	237	283	357
Strong eddies	26 (6.3%)	18 (7.6%)	14 (4.9%)	14 (3.9%)
Regular eddies	389	219	269	343
$F_{HT}$ North [TW]	8.6, [1.6, 11.9]	7.8, [1.4, 10.1]	5.8, [0.9, 9.7]	4.6, [0.6, 7.0]
% by strong eddies	20%	34%	9%	9%
$F_{HS}$ South [TW]	–12.1, [–14.4, –2.1]	–12.8, [–14.5, –2.0]	–10.3, [–11.2, –1.2]	–8.6, [–8.1, –0.7]
% by strong eddies	41%	50%	49%	49%
$\overline{F_H}$ [TW]	–2.1, [–5.6, 3.3]	–2.8, [–4.4, 2.0]	–2.4, [–3.9, 2.4]	–1.9, [–2.0, 1.3]
% by strong eddies <sup>a</sup>	33%	44%	35%	35%
$F_{FW}$ North [mSv]	8.5, [1.6, 10.1]	8.9, [1.4, 10.0]	7.1, [0.9, 7.6]	5.9, [0.5, 5.9]
% by strong eddies	40%	49%	50%	50%
$F_{FW}$ South [mSv]	–6.5, [–8.6, –1.2]	–6.1, [–7.3, –1.1]	–4.3, [–7.2, –0.7]	–3.4, [–5.2, –0.4]
% by strong eddies	21%	35%	8%	8%
$\overline{F_{FW}}$ [mSv]	1.4, [–2.4, 4.0]	1.8, [–1.6, 3.0]	1.4, [–1.7, 2.6]	1.1, [–1.1, 1.4]
% by strong eddies <sup>b</sup>	33%	44%	35%	34%

Note. Negative signs indicate southward transports. The variability shown in brackets represents the inner quartile range (i.e., the range of 50% of the values). See text for the definition of strong eddies.

<sup>a</sup>defined as  $\sum |F_{T, \text{strong}}| / \sum |F_{T, \text{all}}|$ , <sup>b</sup>defined as  $\sum |F_{FW, \text{strong}}| / \sum |F_{FW, \text{all}}|$

zonal section ( $x$ - $z$  plane) through the eddies' center is taken. The dimensions in  $x$  direction are transformed into multiples of the eddy's radius by normalizing the distance from the eddy center with the respective eddy's radius (with a horizontal resolution of  $1/2 R$ ). In order to isolate the eddy signal, the mean stratification is subtracted from each individual section to obtain anomalies of temperature and freshwater. The respective anomalies for CE and AE are averaged to obtain a composite for each sense of rotation.

The vertical structure of eddies crossing 47°N is similar between observations and model simulation. All composites show an asymmetric behavior with more cold and fresh water in the western part of the composite sections. The anomalies induced by the eddies (with exception of the one simulated strong AE) are intensified at the surface but reach down to a depth of around 2,000 m.

In the following, (1) the heat content ( $HC = A \int_{H_E}^0 c_{p_0} [\rho(z) \overline{T'}(z)] dz$ ) and freshwater content ( $FWC = A \int_{H_E}^0 \overline{FW'}(z) dz$ ) of the eddies, (2) the average eddy translation speed ( $\mathbf{v}_E$ ), (3) the eddy radius ( $R_E$ ), and (4) the respective vertical extent ( $H_E$ ) of the eddies are discussed with respect to their contribution to the difference between regular and strong eddies in both observations and the ANHA4-SPG12 simulation. HC and FWC are divided by the respective eddy's area  $A$  and vertical extent  $H_E$  in order to separate between geometrical and thermohaline properties. Respective values are summarized in Table 2.

1. Heat and freshwater content (HC/FWC): A large part of the different transports by regular and strong eddies can be explained by their thermohaline properties. For the period when observations and model overlap (2002–2013), HC falls into the range  $[3.2\text{--}3.6] \times 10^6 \text{ J/m}^3$  for regular and  $[8.1\text{--}10.2] \times 10^6 \text{ J/m}^3$  for strong eddies. Similarly, FWC is in the range  $[2.4\text{--}2.5] \times 10^{-3} \text{ m}^{-3}$  for regular and  $[5.7\text{--}7.2] \times 10^{-3} \text{ m}^{-3}$  for strong eddies (Table 2). The ratio between strong and regular eddies ( $\frac{HC_{\text{regular}}}{HC_{\text{strong}}}$  and  $\frac{FWC_{\text{regular}}}{FWC_{\text{strong}}}$ ) is between 2.2 and 2.9.
2. Translation speed ( $\mathbf{v}_E$ ): The translation speed of regular and strong eddies is the second property explaining the differences between regular and strong eddies. In both observations and model, the translation speed of strong eddies is 3.6 (observations) to 3.7 (model) times faster than for regular eddies.

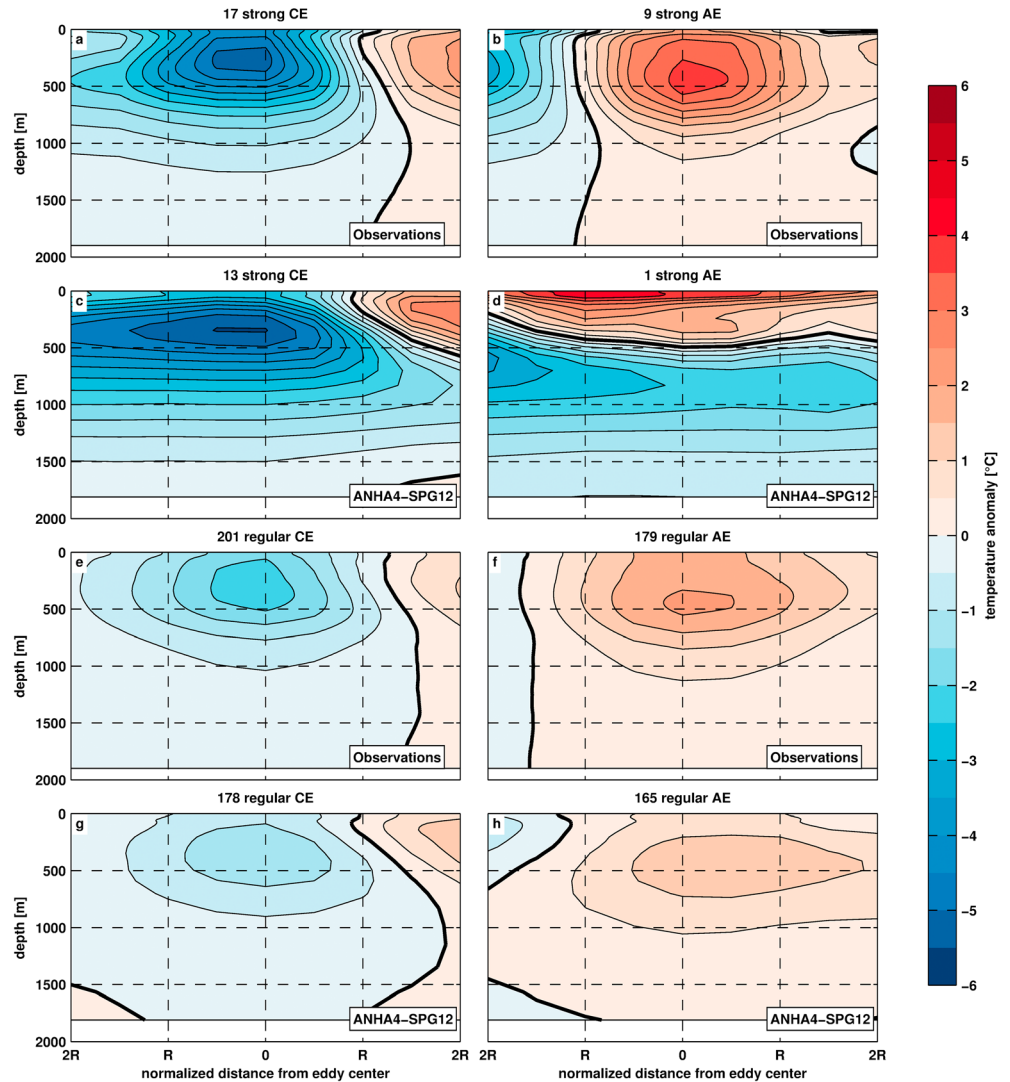


**Figure 7.** Composites of the temperature anomalies associated with eddies crossing 47°N in the observations (January 1993 to April 2014, a/b and e/f) and in the 1/12° ANHA4-SPG12 simulation (January 2002 to December 2013, c/d and g/h). The x axis is given in multiples of eddy radii. The thick black line indicates the zero line. Note that nine regular eddies were too close to the boundary of the GEM region to construct a composite and therefore not considered.

3. Eddy radius ( $R_E$ ): The radius of strong eddies is slightly larger than that of regular eddies for both observations (ratio 1.3) and model simulation (ratio 1.1), which explains only a small fraction of the large differences between regular and strong eddies. As expected, this result is very similar to the surface analysis by Müller et al. (2017).
4. Vertical extent of eddies ( $H_E$ ): The vertical extent is actually smaller for strong eddies than for regular eddies in both, observations and model simulation, and therefore does not explain the large transports by strong eddies.

Overall, the eddy translation speed and the eddies' thermohaline properties (i.e., the temperature and freshwater anomalies of the respective eddies) are the main reasons for the large heat and freshwater transports associated with strong eddies. This agrees well with the result by Müller et al. (2017) that surface temperature fluxes by strong eddies are associated with a larger SST anomaly than fluxes by regular eddies.

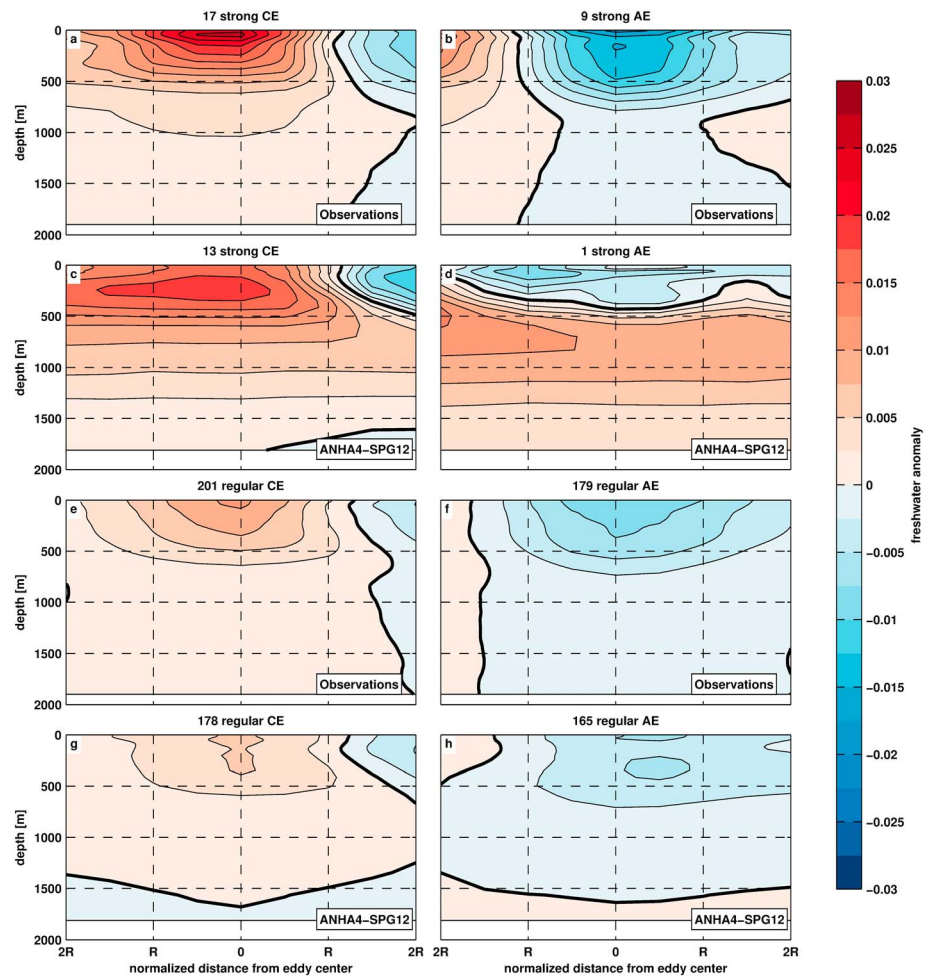


**Figure 8.** Composites of the freshwater anomalies associated with eddies crossing  $47^{\circ}\text{N}$  in the observations (January 1993 to April 2014, a/b and e/f) and in the  $1/12^{\circ}$  ANHA4-SPG12 simulation (January 2002 to December 2013, c/d and g/h). The x axis is given in multiples of eddy radii. The thick black line indicates the zero line. Note that negative freshwater anomalies denote a saline eddy, while positive anomalies indicate fresh eddies. Note that nine regular eddies were too close to the boundary of the GEM region to construct a composite and therefore not considered.

#### 5.4. Spatial Variability of Heat and Freshwater Transports Related to Eddies Crossing $47^{\circ}\text{N}$

In the following, heat and freshwater transports of the eddies crossing  $47^{\circ}\text{N}$  are summed up in bins of  $1^{\circ}$  longitude to obtain a better view on the spatial distribution of the transports carried by eddies (Figures 9 and 10). The terminology is as follows: net transport comprises the sum of all eddies, net regular transport the sum of only regular eddies, and net strong transport the sum of only strong eddies. The number of eddies and the transport are normalized with the length of the respective time series (21 years for the observations, 12 years for the model) to ensure comparability.

There were almost no eddies detected on the Grand Banks in the ANHA4-SPG12 model simulation, and there is no GEM-derived data for regions shallower than 2,000 m. The section analyzed here is therefore reduced to the deep part of the ocean eastward of Flemish Cap (around  $43^{\circ}\text{W}$ ). The eastern basin of the North Atlantic is not completely covered by the GEM field, so we rely on the model simulation for the analysis of this part of the section. We separated the  $47^{\circ}\text{N}$  section into three subsections characterized by different current regimes and different bathymetry, with one subsection in the western boundary region, one around the Mid-Atlantic Ridge (MAR), and one for the eastern basin.

In general, observations and the ANHA4-SPG12 model simulation show very similar results for the pathways of eddies across the  $47^{\circ}\text{N}$  and the related transports of heat and freshwater (Figures 9c/9d

**Table 2**  
Number of Eddies Crossing 47°N and the Respective Properties

Period	Observations		Model (ANHA4-SPG12)	
	Jan 1993 to Apr 2014 (full period)	Jan 2002 to Dec 2013 (period as in the model)	Jan 2002 to Dec 2013 (model period)	Jan 2002 to Dec 2013 (model period)
Zonal extent of the 47°N section	43°W–20.5°W (western and central section)	43°W–20.5°W (western and central section)	43°W–20.5°W (section as in the observations)	53°W–10°W (full section)
Total number of eddies crossing 47°N	415	237	283	357
Strong eddies	26 (6.3%)	18 (7.6%)	14 (4.9%)	14 (3.9%)
Regular eddies	389	219	269	343
eddy radius [km]				
regular eddies	44.9 ± 11.9	45.1 ± 12.7	39.1 ± 10.2	38.3 ± 9.8,
strong eddies	57.2 ± 13.9	58.8 ± 13.6	41.8 ± 7.6	41.8 ± 7.6
transl. speed [cm/s]				
regular eddies	1.7 ± 1.7,	1.5 ± 1.6,	1.9 ± 1.8,	1.7 ± 1.8,
strong eddies	5.1 ± 2.2	5.4 ± 2.3	7.2 ± 2.7	7.2 ± 2.7
vertical extent <sup>a</sup> [m]				
regular eddies	1,340,	1,400,	1,150,	1,150,
strong eddies	1,150	1,160	980	980
HC  [10 <sup>6</sup> J/m <sup>3</sup> ]				
regular eddies	3.5, [1.8, 5.1]	3.2, [1.7, 4.4]	3.6, [1.2, 5.0]	3.0, [0.7, 4.2]
strong eddies	8.1, [6.6, 9.7]	8.1, [5.6, 11.3]	10.2, [10.3, 12.0]	10.2, [10.3, 12.0]
FWC * [10 <sup>-3</sup> m <sup>-3</sup> ]				
regular eddies	2.6, [1.4, 3.7]	2.4, [1.3, 3.3]	2.5, [0.9, 3.6]	2.0, [0.6, 3.1]
strong eddies	5.7, [4.9, 6.8]	5.7, [4.5, 7.7]	7.2, [6.7, 8.4]	7.2, [6.7, 8.4]

Note. The variability shown in brackets represents the inner quartile range (i.e., the range of 50% of the values). The uncertainty of radius and translation speed is given as one standard deviation. See text for the definition of strong eddies.

<sup>a</sup>Median vertical extent, Heat contents (HC) of eddies ( $A \int_{H_E}^0 [\rho(z)T'(z)] dz$ ), and freshwater contents (FWC) of eddies ( $A \int_{H_E}^0 \overline{FW'}(z) dz$ ) are divided by the respective eddy's area  $A$  and vertical extent  $H_E$  in order to separate between geometrical and thermohaline properties:

and 10c/10d). Both reveal high transports in the western basin and very low values compared to that for the remaining 47°N section. To compare the spatial distribution of eddies along 47°N and their respective transports across 47°N, the correlation of the binned values (number of eddies, heat, and freshwater transports) along the section is calculated between observations and model. The correlation coefficient for the numbers of eddies crossing the section is 0.7. Here, the number of eddies in one bin is simply the number of northward moving eddies minus the number of southward moving eddies. The correlation coefficients of the binned transports are higher than 0.9 for both net transports. Overall, the observed features along 47°N, even on scales as small as 1°, are very well reproduced by the 1/12° model simulation.

The heat and freshwater transports of eddies in observations and model confirm the results by Müller et al. (2017), that the western basin is the most important region when it comes to meridional transports by individual eddies crossing 47°N. The western boundary subsection shows the most regular and strong eddies and the highest variability of heat and freshwater transport (Figures 9c/9d and 10c/10d). The directions of the mean (averaged over all eddies crossing the transect) heat transport (southward: -2.8 TW, -2.4 TW in the model) and mean freshwater transport (northward: 1.8 mSv, 1.4 mSv in the model) are determined here. In both observations and model simulation, strong eddies are mostly confined to the NAC with around 90% of all strong eddies crossing 47°N in this region.

Most striking are the three bins, located between 42°W and 40°W, comprising the NAC. Most of the strong eddies found in the western boundary section cross 47°N in this small subsection. The small subsection of only 230-km extent (i.e., less than 1/10 of the full section) accounts for more than 60% of the absolute heat and freshwater transport by eddies across 47°N ( $\sum |F_H|$  and  $\sum |F_{FW}|$ , respectively). These large transports are also accompanied by the highest variability along the section, as expressed by the whiskers in Figures 9c/9d and 10c/10d. The extremely large transports (largest heat and freshwater transports of the whole 47°N section) are caused by cold and fresh eddies moving northward with the NAC.

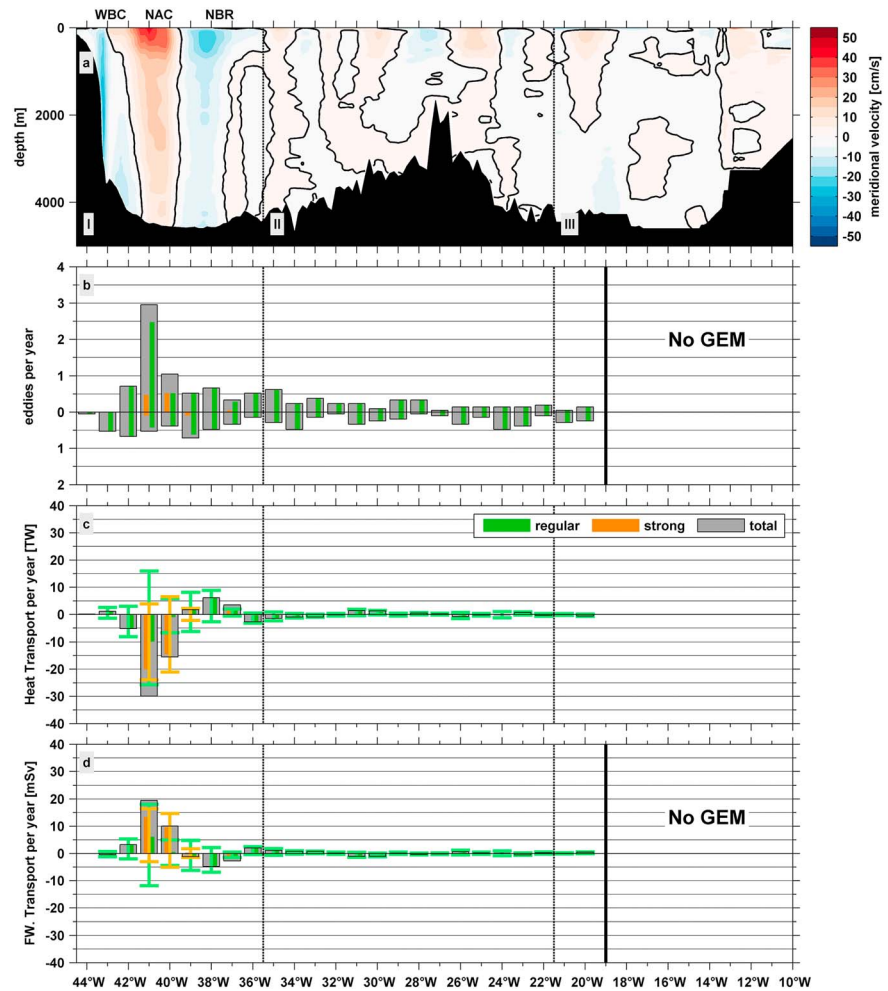


**Figure 9.** (a) Meridional background velocity obtained from 11 sip surveys conducted nominally along 47°N (from Müller et al., 2017), (b) the number of northward and southward moving eddies from satellite observations (January 1993 to April 2014) per 1° bin crossing 47°N per year, and (c) respectively the sum of the heat and freshwater transports (d) by eddies per 1° bin along 47°N (normalized by the number of years). Vertical bars show the sum of the transports of regular (green) and strong (orange) eddies in either direction. The vertical whiskers represent the standard deviation of the respective transports in either direction.

The other bins of the western boundary section show much lower transports by eddies than the three discussed above. The net transports in the WBC are very small compared to the analysis of surface temperature fluxes by Müller et al. (2017), which could be partially due to the fact that the GEM region ends where the water depth is shallower than 2,000 m. In the three bins to the east of the NAC, in the Newfoundland Basin Recirculation (NBR), the transports by eddies observed from satellite observations reverse the sign compared to the NAC region (Figure 9c/9d). The strongest northward heat transport (and southward freshwater transport) coincides with the location of the core of southward velocity of the NBR (Figure 9a). In the model, the NBR is generally weaker, and the reversal of the heat and freshwater transports happens farther east (34°W–38°W) than in the observations (Figure 10c/10d).

As for the surface temperature fluxes by eddies described by Müller et al. (2017), the other subsections play only a minor role for the heat and freshwater transport carried by eddies across 47°N. In both observations and the ANHA4-SPG12 simulation, the net transports and also the variability are much lower there than in the western boundary region (Figures 9c/9d and 10c/10d). The midsection, comprising the MAR, accounts for 11–18% of the respective absolute heat and freshwater transports by eddies.

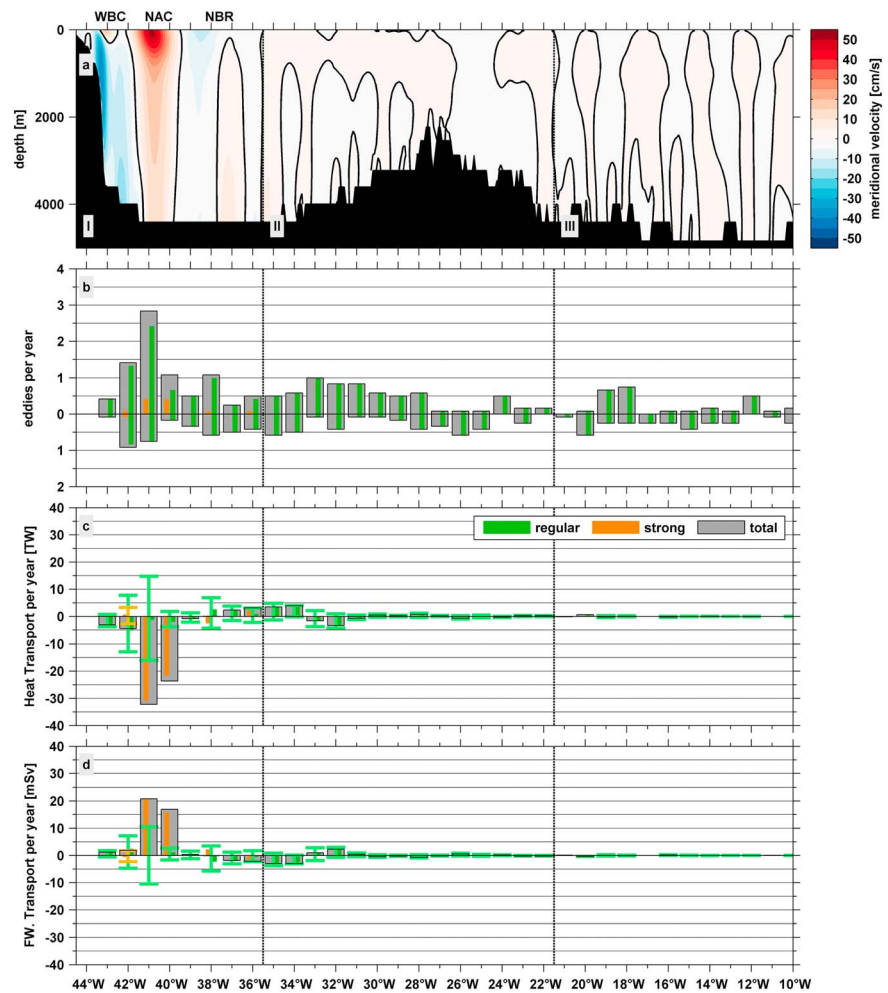


**Figure 10.** (a) Meridional background velocity from the 1/12° ANHA4-SPG12 model simulation as shown in Müller et al. (2017), (b) the number of northward and southward moving eddies from the model simulation (January 2002 to December 2013) per 1° bin crossing 47°N per year, and (c) respectively the sum of the heat and freshwater transports (d) by eddies per 1° bin along 47°N (normalized by the number of years). Vertical bars show the sum of the transports of regular (green) and strong (orange) eddies in either direction. The vertical whiskers represent the standard deviation of the respective transports in either direction.

The eastern basin is not covered by the GEM field, but it has the least contribution to the transport across 47°N in the model simulation. While around 21% of all eddies detected in the model simulation cross 47°N in the eastern basin, these eddies account for only around 2% of the absolute heat and freshwater transports. Also, the surface temperature fluxes by eddies in the eastern basin analyzed by Müller et al. (2017) are almost negligibly small. It is therefore safe to assume that there is no substantial loss to the overall transport by eddies crossing 47°N by not including the eastern basin, and we conclude that the results from the GEM method are representative for the whole 47°N section.

### 5.5. Transports by Individual Eddies Compared to the Turbulent Component of the Flow Field

In the following, we address how much of the total heat and freshwater transport across 47° N can be explained by anomalies carried by eddies, and how much of the turbulent (i.e., the so-called *eddy component*) of the transport can be explained by said anomalies.

The calculation of the heat and freshwater transports across 47° N is straightforward in the model environment. The meridional heat transport is simply

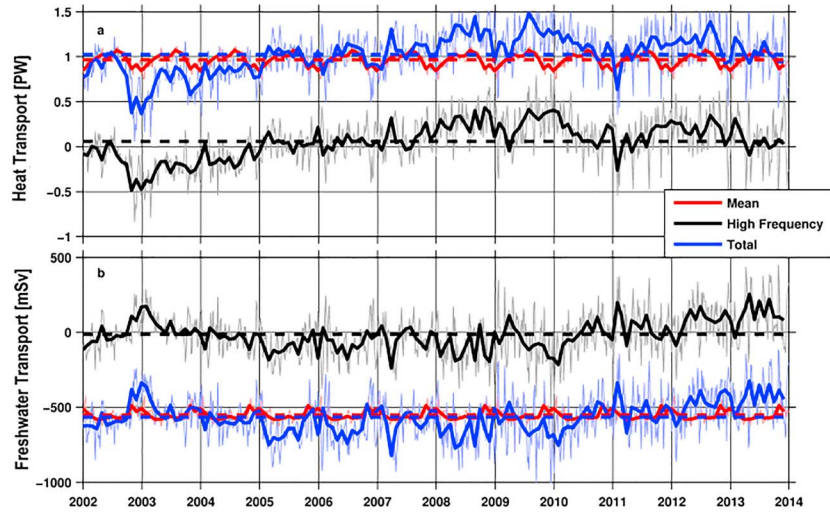


**Figure 11.** Basin wide meridional heat transports (a) and freshwater transports (b) across 47°N in the 1/12°ANHA4-SPG12 model simulation between January 2002 and December 2013. For both transports the monthly mean values (thick lines) and the 5-day model output (thin lines) of the total transport (blue), the mean transport (red), and the high-frequency transport (black) are shown. The respective average values are indicated by dashed lines.

$$F_H = c_{p_0} \rho_0 \int \int v T \, dx dz, \quad [W] \quad (3)$$

and the meridional freshwater transport

$$F_{FW} = \int \int v \, FW \, dx dz, \quad \left[ \frac{m^3}{s} \right] \quad (4)$$

where  $c_{p_0} = 4,200 \, \text{J} \cdot \text{kg}^{-1} \cdot \text{K}^{-1}$  is the average specific heat capacity,  $\rho_0 = 1,025 \, \text{kg/m}^3$  the average seawater density, and  $v$  is the meridional velocity. The full heat and freshwater transports,  $F_H$  and  $F_{FW}$ , are then separated into a *mean component* and a *turbulent component* in the form  $x = x_{\text{mean}} + x_{\text{turb}}$ . For the analysis here, we define the mean component as the part of the flow that is related to the mean annual cycle so that intra-annual changes that are related to the seasonal cycle are captured by the mean components. The mean components of the transports are then  $F_{H\text{mean}} = c_{p_0} \rho_0 \int \int v_{\text{mean}} T_{\text{mean}} \, dx dz$ , and  $F_{FW\text{mean}} = \int \int v_{\text{mean}} FW_{\text{mean}} \, dx dz$ , where  $v_{\text{mean}}$ ,  $T_{\text{mean}}$ , and  $FW_{\text{mean}}$  are the mean annual cycle of the meridional velocity, the temperature, and the freshwater field, respectively. The turbulent components are then simply  $F_{H\text{turb}} = F_H - F_{H\text{mean}}$  and  $F_{FW\text{turb}} = F_{FW} - F_{FW\text{mean}}$  (Figure 11). This means that the turbulent component of the transports includes not only eddies but all variability on intraseasonal scales, like meandering of the major currents, shifts of the temperature front in the Newfoundland Basin, major cooling or warming, and especially the Ekman layer transport. The turbulent component of the respective transports will therefore always be larger than the transports by individual eddies.

The average heat transport across 47°N in the ANHA4-SPG12 model is  $1.0 \pm 0.26$  (one standard deviation) PW, which is high compared to previous observations (Table 3). The turbulent component of that transport is  $0.06 \pm 0.25$  PW. For the freshwater transport, the picture is similar with an average of  $-570 \pm 150$  mSv of which  $-10 \pm 140$  can be explained by the turbulent component. For both cases the turbulent component dominates the variability of the transport, while the strength is defined by the mean component (Figure 11).

To compare the transports by individual eddies with these transports, we cannot simply take the average values from Table 1 (these are the average transports per eddy) calculated with equation (1)–(2). Instead, we sum up the heat/freshwater content of all eddies crossing 47°N (shown in Figure 4) and divide by the length of the time series (in seconds). The mean heat transport by individual eddies in the model is then  $-5.3 \, \text{TW}$  (i.e.,  $-0.005 \, \text{PW}$ ) and the respective mean freshwater transport 3.0 mSv. The transports carried by individual eddies thus range on the order of only  $\mathcal{O}(1/200)$  of the average transports by the

**Table 3**  
Overview on Heat Transport Estimates Across 47°/48°N, Separated Into Total, Turbulent (i.e., Eddy Component), and the Transport Carried by Individual Eddies

Reference		Total heat transport	Turbulent component	Heat transport carried by individual eddies
Macdonald (1998; ship section and inverse model)		$0.65 \pm 0.25$ PW	---	---
Ganachaud and Wunsch (2003)* (ship section and inverse model)		$0.6 \pm 0.1$ PW	---	---
Lumpkin and Speer (2007)* (ship section and inverse model)		$0.61 \pm 0.13$ PW	---	---
Lumpkin et al. (2008)* (repeated ship observations and inverse model)		$0.53 \pm 0.04$ PW	---	---
Rhein et al. (2011; 1/12° model study)		$0.7 \pm 0.2$ PW	$0.01 \pm 0.1$ PW	---
This study	1/12° model	$1.0 \pm 0.3$ PW	$0.06 \pm 0.3$ PW	$-0.005 \pm 0.03$ PW
	observations	---	---	$-0.004 \pm 0.1$ PW

\*These studies address the former WOCE-line A2/AR19 as the 48°N section. This section follows the 47°N section used here along its eastern part, while it starts farther south in the Newfoundland Basin.

background flow. However, the variability of the transports by individual eddies is higher ( $\pm 0.03$  PW and  $\pm 19$  mSv), explaining 10–13% of the overall variability.

As our available subsurface observational velocity data are limited to individual ship surveys, we cannot infer similar heat transport time series from these observations. We therefore refer to estimates provided by other studies (Table 3). Different studies (e.g., Ganachaud & Wunsch, 2003; Lumpkin et al., 2008; Macdonald, 1998; Rhein et al., 2011) using ship observations or numerical models have quantified the heat transport at 47°N to about 0.6 PW with a standard deviation on the order of 0.1–0.2 PW. Rhein et al. (2011) showed that at least in their 1/12° model, the turbulent component makes up around 60% of the variability ( $\sim 0.1$  PW), while the mean turbulent transport is negligible (0.01 PW). The observed transports by individual eddies fall very well into this range. The mean heat transport by eddies is negative ( $-0.004$  PW) but negligibly small compared to the mean transport. The standard deviation ( $\pm 0.1$  PW) is the same as in the study by Rhein et al. (2011), explaining most of the observed variability.

Unlike other eddies, for example, Agulhas Rings (e.g., Beal et al., 2011) or North Brazil Current Rings (e.g., Goni & Johns, 2001), net transports by individual eddies crossing 47°N are negligible compared to the transports by the mean flow across 47°N and even small compared to the turbulent component of the respective transports. They do, however, have a notable influence on the variability of the average transports. Transports of individual eddies account for around 60% of the overall variability in the observation and around 10–15% in the ANHA4-SPG12 model simulation.

## 6. Discussion

One major finding is the considerable impact of northward moving cold and fresh cyclones compared to the transport by other eddies. Two types of eddies account for a northward heat and a southward freshwater transport (warm and salty northward and cold and fresh southward), and two types of eddies account for a southward heat and a northward freshwater transport (cold and fresh northward and warm and salty southward). In both observations and model around 30% of the eddies crossing 47°N are cold and fresh northward moving eddies. Most of the strong eddies (16/26 for the observations and 12/14 for the model) also fall into this category. The exceptional role of these eddies becomes obvious when comparing the cumulative sums of the four major different types (Figure 12). For both observations and ANHA4-SPG12 model simulation, the cumulative transport of these eddies stands out and exceeds all other types (red lines in Figure 12).

The other three types are associated with transports of approximately the same magnitude (apart from opposing signs of course). Comparing the slopes of the lines shows that the cumulative transport of observed cold and fresh eddies is between 1.6 and 3.6 (average: 2.5) times higher than that of other eddies. For the ANHA4-SPG12 model simulation the effect is even stronger, and the cumulative transport of cold and fresh eddies is between 2.5 and 6.5 (average: 3.8) times higher than that of other eddies. The large cumulative effect is caused on the one hand by the high number of cold and fresh eddies moving northward and on the other hand by their larger than average heat and freshwater contents. Their average HC/FWC

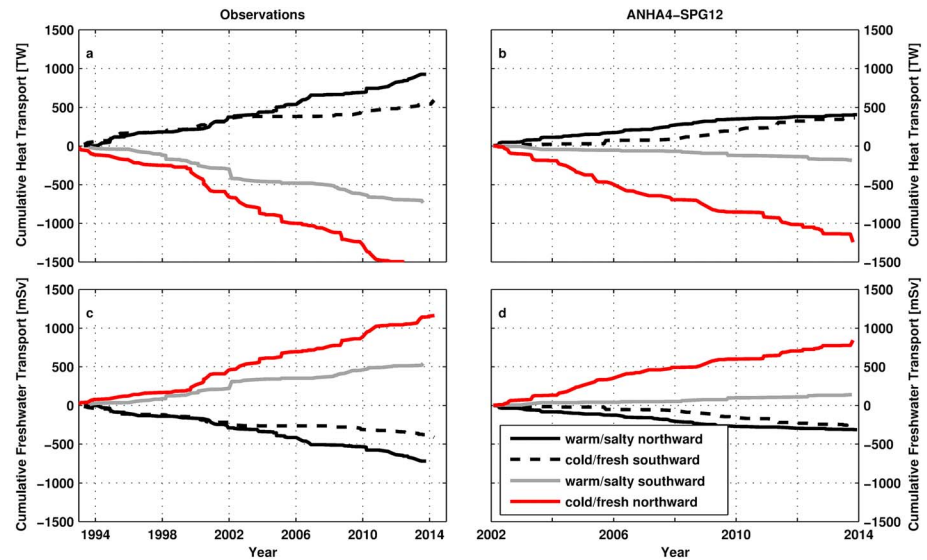


**Figure 12.** Cumulative sum of the heat (a/b) and freshwater (c/d) transports by eddies for the four major types of eddies for the observations (left) and the 1/12° ANHA4-SPG12 model simulation (right). The four major eddy types make up 98% of all eddies in the observations and 99% of all eddies in the model simulation. Note the different length of the time series for observations and model and the different scales on the Y axis.

(divided by the respective eddy's area  $A$  and vertical extent  $H_E$ ) is between 1.5 and 2.1 times larger than that of other eddies (1.2–1.9 times larger for only regular eddies).

Another important point concerns the travel distance of eddies and the question whether the effects of heat and freshwater transports by eddies across 47°N are mostly local or also notable on larger regional scales. In other regions of the world, large coherent eddies can carry water for very long distances (e.g., Agulhas Rings; Beal et al., 2011; or North Brazil Current Rings; Goni & Johns, 2001), playing a crucial role for the large scale distribution of water masses. However, eddies crossing 47°N are smaller and the average travel distance of eddies after crossing 47°N is around 80 km, with about 1/3 of all eddies traveling farther than 100 km and individual eddies traveling up to 300 km (Müller et al., 2017). The effect of heat and freshwater transports by eddies crossing 47°N is therefore much more locally confined, than, for example, the freshwater transport by North Brazil Current Rings (e.g., Goni & Johns, 2001). Nonetheless, the local effects of eddies crossing 47°N are far from negligible and eddies play a considerable role for the local variability of the heat and freshwater transports across 47°N.

Eddies in the Newfoundland Basin also provide a means of exchange between WBC and NAC. Pérez-Brunius et al. (2004) used historical hydrographic data in combination with isopycnal RAFOS float data from the area and found that the heat loss of the NAC in the western subpolar North Atlantic is caused mostly by horizontal cross-frontal exchange induced by the eddy field. They suggest that steep meanders of the NAC are the main reason for this exchange. The heat loss by horizontal exchange is 10 times greater than the vertical heat loss to the atmosphere and the largest losses occur south of the Grand Banks and around 47°N in the Newfoundland Basin (Pérez-Brunius et al., 2004, their Figure 9). Saenko (2015) found similar results using a 1/12° configuration of the NEMO model (Madec, 2008). His results suggest that the convergence of heat brought into the Newfoundland Basin with the mean flow of the NAC is 2–3 times larger than the heat loss to the atmosphere. The excessive heat is compensated by a strong cooling effect due to lateral turbulent heat transports. Bower et al. (2009) tracked RAFOS floats released in the WBC around 50°N and found that most floats leave the WBC somewhere between Flemish Cap at 47°N and the Tail of the Grand Banks around 42°N. Their results show that cold water detaching with eddies from the WBC (suggested by the spiraling of the float trajectories) sometimes remains in the NAC pathway (Bower et al., 2009).

The present study fits in well with the results by Pérez-Brunius et al. (2004), Bower et al. (2009), and Saenko (2015). We have identified cold and fresh eddies detaching from the WBC as an additional source for the

**Table 4**  
Overview of the Results of the Different Methods Used in This Study

Result	Surface (Müller et al., 2017)			3-D (this study)	
	Observations (1/4°)	ANHA4 (1/4°)	ANHA4-SPG12 (1/12°)	GEM (1/4°)	ANHA4-SPG12 (1/12°)
Large fraction of absolute transports by strong eddies	Y	Y	Y	Y	Y
Difference between regular and strong due to thermohaline properties	Y	Y	Y	Y	Y
Pathways of eddies related to main current branches	Y	Y	Y	Y	Y
Large contribution by cold/fresh cyclones	Y	N	Y	Y	Y
Southward temperature/heat transport in the NAC region	Y	N	Y	Y	Y
Northward freshwater transport in the NAC region	---	---	---	Y	Y
Overall net southward temperature/heat transport	N	N	Y	Y	Y
Overall northward freshwater transport	---	---	---	Y	Y
Transports in eastern basin negligible	Y	Y	Y	<b>not fully resolved</b>	Y

Note. The **Y** indicates that the result is confirmed by the respective method, the **N** indicates that the result is not confirmed.

cooling of the NAC around Flemish Cap. The increased atmosphere-ocean interaction over mesoscale eddies (e.g., Ma et al., 2016) is also likely to play a role for the strong cooling of the NAC in the Newfoundland Basin.

The eddy detection algorithm used in this study was designed to be a reliable tool for distinguishing between meanders and eddies (Nencioli et al., 2010). Escudier et al. (2016) compared different eddy detection algorithms and showed that eddies detected with the vector-geometry-based algorithm are, in general, somewhat smaller than eddies detected with other methods. A comparison with eddy data retrieved from the META data set (*Mesoscale Eddy Trajectory Atlas*, version 1.0exp; SSALTO/Duacs, 2017) showed that the algorithm used here can differentiate between different small features and shows consistent outer boundaries for the detected eddies. We also analyzed eddy trajectories (not shown) and found them to be somewhat shorter than the trajectories derived with other algorithms. As was observed by Escudier et al. (2016), the detected eddies here are somewhat small when compared to the velocity field, which could be a source for a systematic underestimation of the transports by eddies.

## 7. Conclusions

The results from the analysis of the heat and freshwater transports by eddies crossing 47°N agree with the results from the surface temperature fluxes analyzed by Müller et al. (2017). Table 4 gives an overview of the different analyses carried out in the two studies and the respective main results.

Using a combination of 21 years of geostrophic surface velocities from satellite altimetry, surface and subsurface temperature and salinity data constructed from surface parameters using the GEM method, ship-based velocity measurements, and a high-resolution (1/12°) simulation with the NEMO ocean model spanning a period of 12 years, we have found:

1. Despite the limitations at 47°N, the GEM method is a suitable technique to reconstruct 3-D thermohaline fields from sea surface height observations combined with Argo data that are well resolved in space and time. These fields contain clear enough information allowing to infer heat and freshwater transports associated with individual eddies (Figures 4 and 5).
2. In both, observations and ANHA4-SPG12 model simulation, so-called strong eddies have a 2–3 times higher heat content and freshwater content than so-called regular eddies (Figures 7 and 8 and Table 2).
3. About 45% of the observed absolute heat and freshwater transports by eddies across 47°N stem from strong eddies. In the ANHA4-SPG12 model around one third of the respective transports stem from strong eddies (Table 1).
4. Fluxes by eddies are largest in the western part of the Newfoundland Basin, and northward moving cold and fresh cyclones carrying subpolar water from the WBC make a considerable contribution to the overall heat and freshwater transports by eddies (Figures 9, 10, and 12).
5. Despite the GEM-derived hydrographic fields not fully covering the eastern basin of the North Atlantic at 47°N, this region could be studied more closely with the model simulation. Results showed that this

#### Acknowledgments

This study was supported by the Deutsche Forschungsgemeinschaft (DFG) through the International Research Training Group Processes and impacts of climate change in the North Atlantic Ocean and the Canadian Arctic (IRTG 1904 ArcTrain, V. M. and D.K.) and by the Cluster of Excellence The Oceans in the Earth System MARUM, subproject OC-1 (D. K.), funded by the DFG. Support for the cruises came from the Co-Operative Project RACE-Regional Atlantic Circulation and Global Change, Grant 03F0651C, and Co-Operative Project Nordatlantik, Grants 03F0443C and 03F0605, all funded by the German Federal Ministry of Education and Research (BMBF), as well as the DFG through the Senate Commission on Oceanography. I. S. and R. S. were supported by the DFG research Units 1740: Atlantic Freshwater Cycle (Grant RH 25/40-2). P. G. M. and C. P. gratefully acknowledge the financial and logistic support of grants from the Natural Sciences and Engineering Research Council (NSERC) of Canada. These include a Discovery Grant (rgpin 227438-09), Climate Change and Atmospheric Research Grant (VITALS-RGPPC 433898), and an International Create (ArcTrain 432295). The altimeter products were produced by Ssalto/Duacs and distributed by AVISO, with support from CNES (<http://www.aviso.altimetry.fr/duacs/>). Argo data were collected and made freely available by the International Argo Program and the national programs that contribute to it (<http://www.argo.ucsd.edu> and <http://argo.jcom-mops.org>). The Argo Program is part of the Global Ocean Observing System. We thank Birgit Klein, Federal Maritime, and Hydrographic Agency (BSH), Hamburg, Germany, for providing quality-controlled Argo data from the North Atlantic. This subset was downloaded from the Coriolis data center. The Mesoscale Eddy Trajectory Atlas products were produced by SSALTO/DUACS and distributed by AVISO+ (<https://www.aviso.altimetry.fr>) with support from CNES, in collaboration with Oregon State University with support from NASA. The research of this study was enabled in part by support provided by WestGrid ([www.westgrid.ca](http://www.westgrid.ca)) and Compute Canada ([www.compute-canada.ca](http://www.compute-canada.ca)). We thank Francesco Nencioli (Plymouth, UK) for his helpful advice on using the eddy detection algorithm and Xianmin Hu (now at BIO, Dartmouth, Canada) for his help with the model simulations. We also thank the anonymous reviewer for improving the manuscript.

region contributes only a small part to the meridional heat and freshwater transports carried by eddies across 47°N (Figures 9 and 10).

- The spatial patterns of the number of eddies crossing 47°N, as well as the patterns of the heat and the freshwater transports carried by those eddies across 47°N, are consistent between the observations and the ANHA4-SPG12 model simulation (correlations between 0.7 and 0.9, Figures 9 and 10).
- The contribution of eddies to the average heat transport across 47°N is negligible. However, eddies account for a considerable part of the temporal variability of the transports.

Overall, the results from this study provide a better understanding of the contribution of eddies to the transports of heat and freshwater and their variability in a region that is of great relevance for the climate system. The consistency between the two independent data sets, observations, and model simulation shows that the results produced with the GEM method and inferred from the model are both physically meaningful. While there are still limitations regarding the availability of high-quality observations that are well resolved in space and time, model simulations that reasonably well reflect mesoscale dynamics can be used to study thermohaline transports by eddies in regions that may be less well covered by observations.

#### References

- Amante, C., & Eakins, B. W. (2009). ETOPO1 1 arc-minute global relief model: Procedures, data sources and analysis. NOAA Technical Memorandum NESDIS NGDC-24. National Geophysical Data Center, NOAA. <https://doi.org/10.1594/PANGAEA.769615>
- Amores, A., Melnichenko, O., & Maximenko, N. (2017). Coherent mesoscale eddies in the North Atlantic subtropical gyre: 3-D structure and transport with application to the salinity maximum. *Journal of Geophysical Research: Oceans*, 122, 23–41. <https://doi.org/10.1002/2016JC012256>
- Argo. (2000). Argo float data and metadata from Global Data Assembly Centre (Argo GDAC). SEANOE. <https://doi.org/10.17882/42182>
- Beal, L. M., De Ruijter, W. P. M., Biastoch, A., & Zahn, R. (2011). On the role of the Agulhas system in ocean circulation and climate. *Nature*, 472(7344), 429–436. <https://doi.org/10.1038/nature09983>
- Bower, A. S., Hendry, R. M., Amrhein, D. E., & Lilly, J. M. (2013). Direct observations of formation and propagation of subpolar eddies into the Subtropical North Atlantic. *Deep-sea research. Part II: Topical studies in oceanography*, 85, 15–41. <https://doi.org/10.1016/j.dsr2.2012.07.029>
- Bower, A. S., Lozier, M. S., Gary, S. F., & Böning, C. W. (2009). Interior pathways of the North Atlantic meridional overturning circulation. *Nature*, 459(7244), 243–247. <https://doi.org/10.1038/nature07979>
- Chaigneau, A., Eldin, G., & Dewitte, B. (2009). Eddy activity in the four major upwelling systems from satellite altimetry (1992–2007). *Progress in Oceanography*, 83(1–4), 117–123. <https://doi.org/10.1016/j.pocean.2009.07.012>
- Chaigneau, A., Gizolme, A., & Grados, C. (2008). Mesoscale eddies off Peru in altimeter records: Identification algorithms and eddy spatio-temporal patterns. *Progress in Oceanography*, 79(2–4), 106–119. <https://doi.org/10.1016/j.pocean.2008.10.013>
- Chaigneau, A., Le Texier, M., Eldin, G., Grados, C., & Pizarro, O. (2011). Vertical structure of mesoscale eddies in the eastern South Pacific Ocean: A composite analysis from altimetry and Argo profiling floats. *Journal of Geophysical Research*, 116, C11025. <https://doi.org/10.1029/2011JC007134>
- Chelton, D. B., Schlax, M. G., & Samelson, R. M. (2011). Global observations of nonlinear mesoscale eddies. *Progress in Oceanography*, 91(2), 167–216. <https://doi.org/10.1016/j.pocean.2011.01.002>
- Dai, A., Qian, T., Trenberth, K. E., & Milliman, J. D. (2009). Changes in continental freshwater discharge from 1948 to 2004. *Journal of Climate*, 22(10), 2773–2792. <https://doi.org/10.1175/2008JCLI2592.1>
- Debreu, L., Vouland, C., & Blayo, E. (2008). AGRIF: Adaptive grid refinement in Fortran. *Computers and Geosciences*, 34(1), 8–13. <https://doi.org/10.1016/j.cageo.2007.01.009>
- Dickson, R., Rudels, B., Dye, S., Karcher, M., Meincke, J., & Yashayaev, I. (2007). Current estimates of freshwater flux through Arctic and subarctic seas. *Progress in Oceanography*, 73(3–4), 210–230. <https://doi.org/10.1016/j.pocean.2006.12.003>
- Dong, C., McWilliams, J. C., Liu, Y., & Chen, D. (2014). Global heat and salt transports by eddy movement. *Nature Communications*, 5(1). <https://doi.org/10.1038/ncomms4294>
- Dong, D., Brandt, P., Chang, P., Schütte, F., Yang, X., Yan, J., & Zeng, J. (2017). Mesoscale eddies in the northwestern Pacific Ocean: Three-dimensional eddy structures and heat/salt transports. *Journal of Geophysical Research: Oceans*, 122, 9795–9813. <https://doi.org/10.1002/2017JC013303>
- Ducet, N., Le Traon, P. Y., & Reverdin, G. (2000). Global high-resolution mapping of ocean circulation from TOPEX/Poseidon and ERS-1 and -2. *Journal of Geophysical Research*, 105(C8), 19,477–19,498. <https://doi.org/10.1029/2000JC900063>
- Dutkiewicz, S., Rothstein, L., & Rossby, T. (2001). Pathways of cross-frontal exchange in the North Atlantic Current. *Journal of Geophysical Research*, 106(C11), 26917–26928. <https://doi.org/10.1029/1999JC000089>
- Escudier, R., Renault, L., Pascual, A., Brasseur, P., Chelton, D., & Beuvier, J. (2016). Eddy properties in the Western Mediterranean Sea from satellite altimetry and a numerical simulation. *Journal of Geophysical Research: Oceans*, 121, 3990–4006. <https://doi.org/10.1002/2015JC011371>
- Ferry, N., Parent, L., Garric, G., Barnier, B., & Jourdain, N. C. (2010). Mercator global Eddy permitting ocean reanalysis GLORYS1V1: Description and results. *Mercator-Ocean Quarterly Newsletter*, 34, 15–27.
- Fichefet, T., & Maqueda, M. A. M. (1997). Sensitivity of a global sea ice model to the treatment of ice thermodynamics and dynamics. *Journal of Geophysical Research*, 102(C6), 12609–12646. <https://doi.org/10.1029/97JC00480>
- Ganachaud, A., & Wunsch, C. (2003). Large-scale ocean heat and freshwater transports during the world ocean circulation experiment. *Journal of Climate*, 16(4), 696–705. [https://doi.org/10.1175/1520-0442\(2003\)016<0696:LSOHAF>2.0.CO;2](https://doi.org/10.1175/1520-0442(2003)016<0696:LSOHAF>2.0.CO;2)
- Goni, G. J., & Johns, W. E. (2001). A census of North Brazil current rings observed from TOPEX/POSEIDON altimetry: 1992–1998. *Geophysical Research Letters*, 28(1), 1–4. <https://doi.org/10.1029/2000GL011717>

- He, Q., Zhan, H., Cai, S., He, Y., Huang, G., & Zhan, W. (2018). A new assessment of mesoscale eddies in the South China Sea: Surface features, three-dimensional structures, and thermohaline transports. *Journal of Geophysical Research: Oceans*, *123*, 4906–4929. <https://doi.org/10.1029/2018JC014054>
- Hunke, E. C., & Dukowicz, J. K. (1997). An elastic-viscous-plastic model for sea ice dynamics. *Journal of Physical Oceanography*, *27*(9), 1849–1867. <https://doi.org/10.1175/1520-0485>
- Keppler, L., Cravatte, S., Chaigneau, A., Pegliasco, C., Gourdeau, L., & Singh, A. (2018). Observed characteristics and vertical structure of mesoscale eddies in the southwest tropical Pacific. *Journal of Geophysical Research: Oceans*, *123*, 2731–2756. <https://doi.org/10.1002/2017JC013712>
- Kieke, D., Klein, B., Stramma, L., Rhein, M., & Koltermann, K. P. (2009). Variability and propagation of Labrador Sea Water in the southern subpolar North Atlantic. *Deep-sea research. Part I: Oceanographic research papers*, *56*(10), 1656–1674. <https://doi.org/10.1016/j.dsr.2009.05.010>
- Le Traon, P. Y., Nadal, F., & Ducet, N. (1998). An improved mapping method of multisatellite altimeter data. *Journal of Atmospheric and Oceanic Technology*, *15*(2), 522–534. [https://doi.org/10.1175/1520-0426\(1998\)015<0522:AIMMOM>2.0.CO;2](https://doi.org/10.1175/1520-0426(1998)015<0522:AIMMOM>2.0.CO;2)
- Liu, Y., Dong, C., Guan, Y., Chen, D., McWilliams, J., & Nencioli, F. (2012). Eddy analysis in the subtropical zonal band of the North Pacific Ocean. *Deep-Sea Research Part I: Oceanographic Research Papers*, *68*, 54–67. <https://doi.org/10.1016/j.dsr.2012.06.001>
- Lumpkin, R., & Speer, K. (2007). Global ocean meridional overturning. *Journal of Physical Oceanography*, *37*(10), 2550–2562. <https://doi.org/10.1175/JPO3130.1>
- Lumpkin, R., Speer, K. G., & Koltermann, K. P. (2008). Transport across 48°N in the Atlantic Ocean. *Journal of Physical Oceanography*, *38*(4), 733–752. <https://doi.org/10.1175/2007JPO3636.1>
- Ma, X., Jing, Z., Chang, P., Liu, X., Montuoro, R., Small, R. J., et al. (2016). Western boundary currents regulated by interaction between ocean eddies and the atmosphere. *Nature*, *535*(7613), 533–537. <https://doi.org/10.1038/nature18640>
- Macdonald, A. M. (1998). The global ocean circulation: A hydrographic estimate and regional analysis. *Progress in Oceanography*, *41*(3), 281–382. [https://doi.org/10.1016/S0079-6611\(98\)00020-2](https://doi.org/10.1016/S0079-6611(98)00020-2)
- Madec, G. (2008). NEMO ocean engine. *Note Du Pôle de Modélisation, Institut Pierre-Simon Laplace (IPSL)*, *27*(27), 357 pp. Retrieved from <http://eprints.soton.ac.uk/64324/>
- Meijers, A. J. S., Bindoff, N. L., & Rintoul, S. R. (2011). Estimating the four-dimensional structure of the southern ocean using satellite altimetry. *Journal of Atmospheric and Oceanic Technology*, *28*(4), 548–568. <https://doi.org/10.1175/2010JTECHO790.1>
- Meinen, C. S., & Watts, D. R. (2000). Vertical structure and transport on a transect across the North Atlantic Current near 42°N: Time series and mean. *Journal of Geophysical Research*, *105*(C9), 21,869–21,891. <https://doi.org/10.1029/2000JC900097>
- Melnichenko, O., Amores, A., Maximenko, N., Hacker, P., & Potemra, J. (2017). Signature of mesoscale eddies in satellite sea surface salinity data. *Journal of Geophysical Research: Oceans*, *122*, 1416–1424. <https://doi.org/10.1002/2016JC012420>
- Mertz, G., Narayanan, S., & Helbig, J. (1993). The freshwater transport of the Labrador current. *Atmosphere-Ocean*, *31*(2), 281–295. <https://doi.org/10.1080/07055900.1993.9649472>
- Müller, V., Kieke, D., Myers, P. G., Pennelly, C., & Mertens, C. (2017). Temperature flux carried by individual eddies across 47°N in the Atlantic Ocean. *Journal of Geophysical Research: Oceans*, *122*, 2441–2464. <https://doi.org/10.1002/2016JC012175>
- Nencioli, F., Dong, C., Dickey, T., Washburn, L., & McWilliams, J. C. (2010). A vector geometry-based eddy detection algorithm and its application to a high-resolution numerical model product and high-frequency radar surface velocities in the Southern California Bight. *Journal of Atmospheric and Oceanic Technology*, *27*(3), 564–579. <https://doi.org/10.1175/2009JTECHO725.1>
- Pegliasco, C., Chaigneau, A., & Morrow, R. (2015). Main eddy vertical structures observed in the four major Eastern Boundary Upwelling Systems. *Journal of Geophysical Research: Oceans*, *120*, 6008–6033. <https://doi.org/10.1002/2015JC010950>
- Pérez-Brunius, P., Rossby, T., & Watts, D. R. (2004). Absolute transports of mass and temperature for the North Atlantic Current-Subpolar Front System. *Journal of Physical Oceanography*, *34*(8), 1870–1883. [https://doi.org/10.1175/1520-0485\(2004\)034<1870:ATOMAT>2.0.CO;2](https://doi.org/10.1175/1520-0485(2004)034<1870:ATOMAT>2.0.CO;2)
- Rhein, M., Kieke, D., Hüttl-Kabus, S., Roessler, A., Mertens, C., Meissner, R., et al. (2011). Deep water formation, the subpolar gyre, and the meridional overturning circulation in the subpolar North Atlantic. *Deep-Sea Research Part II: Topical Studies in Oceanography*, *58*(17–18), 1819–1832. <https://doi.org/10.1016/j.dsr2.2010.10.061>
- Robinson, A. R. (1983). In A. R. Robinson (Ed.), *Eddies in marine science*. Berlin, Heidelberg: Springer Berlin Heidelberg. <https://doi.org/10.1007/978-3-642-69003-7>
- Roessler, A., Rhein, M., Kieke, D., & Mertens, C. (2015). Long-term observations of North Atlantic Current transport at the gateway between western and eastern Atlantic. *Journal of Geophysical Research: Oceans*, *120*, 4003–4027. <https://doi.org/10.1002/2014JC010662>
- Saenko, O. A. (2015). Strong eddy compensation for the Gulf Stream heat transport. *Geophysical Research Letters*, *42*, 10739–10744. <https://doi.org/10.1002/2015GL066111>
- Smith, G. C., Roy, F., Mann, P., Dupont, F., Brasnett, B., Lemieux, J.-F., et al. (2014). A new atmospheric dataset for forcing ice-ocean models: Evaluation of reforecasts using the Canadian global deterministic prediction system. *Quarterly Journal of the Royal Meteorological Society*, *140*(680), 881–894. <https://doi.org/10.1002/qj.2194>
- SSALTO/Duacs. (2014). A new version of SSALTO/Duacs products available in April 2014 (Vol. 1.1). Retrieved from <http://www.aviso.altimetry.fr/fileadmin/documents/data/duacs/Duacs2014.pdf>
- SSALTO/Duacs. (2017). Mesoscale eddy trajectory atlas product handbook. Ramonville St Agne, France. Retrieved from [https://www.aviso.altimetry.fr/fileadmin/documents/data/tools/hdbk\\_eddytrajectory.pdf](https://www.aviso.altimetry.fr/fileadmin/documents/data/tools/hdbk_eddytrajectory.pdf)
- Stendardo, I., Rhein, M., & Hollmann, R. (2016). A high resolution salinity time series 1993–2012 in the North Atlantic from Argo and Altimeter data. *Journal of Geophysical Research: Oceans*, *121*, 2523–2551. <https://doi.org/10.1002/2015JC011439>
- Swart, S., Speich, S., Ansong, I. J., & Lutjeharms, J. R. E. (2010). An altimetry-based gravest empirical mode south of Africa: 1. Development and validation. *Journal of Geophysical Research*, *115*, C03002. <https://doi.org/10.1029/2009JC005299>
- Waugh, D. W., & Abraham, E. R. (2008). Stirring in the global surface ocean. *Geophysical Research Letters*, *35*, L20605. <https://doi.org/10.1029/2008GL035526>
- Wunsch, C. (1999). Where do ocean eddy heat fluxes matter? *Journal of Geophysical Research*, *104*(C6), 13,235–13,249. <https://doi.org/10.1029/1999JC900062>
- Zhang, Z., Wang, W., & Qiu, B. B. (2014). Oceanic mass transport by mesoscale eddies. *Science*, *345*(6194), 322–324. <https://doi.org/10.1126/science.1252418>